Earth Planet. Sci. Lett. 644 (2024) 118830

Contents lists available at ScienceDirect

Earth and Planetary Science Letters

journal homepage: www.elsevier.com/locate/epsl

The impact of climate on relief in the northern Japanese Alps within the past 1 Myr–The case of the Tateyama mountains

M. Bartz [a,*], G.E. King [a], M. Bernard [a], F. Herman [a], X. Wen [a], S. Sueoka [b], S. Tsukamoto [c,d], J. Braun [e,f], T. Tagami [g]

[a] Institute of Earth Surface Dynamics, University of Lausanne, Switzerland
[b] Tono Geoscience Center, Japan Atomic Energy Agency, Japan
[c] Leibniz Institute for Applied Geophysics, Hanover, Germany
[d] Department of Geosciences, University of Tübingen, Germany
[e] Helmholtz Centre Potsdam, GFZ German Research Centre for Geosciences, Potsdam, Germany
[f] Institute of Earth and Environmental Sciences, University of Potsdam, Potsdam, Germany
[g] Graduate School of Science, Kyoto University, Japan

ARTICLE INFO

Editor: Dr A Webb

Keywords:
Rock cooling
Erosion
Quaternary
Electron spin resonance
Luminescence
Japanese islands

ABSTRACT

The impact of climate on mountain relief is often questioned, mainly due to the difficulties of measuring surface processes at the timescale of glacial-interglacial cycles. An appropriate setting for studying mountain erosion in response to Quaternary climate change is found in the Tateyama mountains in the Hida mountain range (northern Japanese Alps) due to distinct geomorphological features. The Japanese Alps uplifted within the past ~1–3 Myr and experienced multiple glaciations during the late Quaternary. We use ultra-low temperature thermochronometers based on the luminescence of feldspar minerals from 19 rock samples and the electron spin resonance (ESR) of quartz minerals from 8 rock samples, in combination with inverse modelling to derive rock cooling rates and exhumation rate histories at 10^4–10^6 year timescales from three transects in the Tateyama region. While luminescence signals have already reached their upper dating limit, ESR signals (Al and Ti centres) yielded ESR ages of ~0.3–1.1 Ma, implying surface processes active in the Pleistocene. Based on a negative age-elevation relationship, local relief reduction at a cirque-basin scale is identified over the past 1 Myr, whereas a positive age distribution with elevation for samples close to the mountain top does not follow this trend. Inverse modelling reveals rock cooling rates on the order of 20–70 °C/Myr, with slightly faster cooling for cirque-floor samples, which equate with erosion rates of 0.5–1 mm/yr that exceed rates from periglacial and slope processes in the same locality. Thus, our data suggest that Quaternary climate change coupled with distinct surface processes modified the slopes of the Tateyama mountains leading to a localised decrease in relief within an individual cirque basin over the second half of the Quaternary.

1. Introduction

The interaction between rates of Earth surface processes, climate and tectonics determines the landscape in mountainous regions. Japan is one of the most tectonically active regions on Earth due to its location at the convergence zones between four tectonic plates (Taira, 2001). The most extensive mountain range, the Japanese Alps, uplifted throughout the Quaternary and reaches elevations up to 3000 m (Harayama et al., 2003). In addition to tectonically driven changes in topography, westerly winds and the winter monsoon (e.g., Takeuchi et al. 2008) result in very high rates of precipitation at high altitudes and significant snow accumulations (6–10 m/yr; Osada et al., 2004). The Hida mountain range (HMR) and Kiso range of the Japanese Alps were glaciated during marine isotope stage (MIS) 4/3 and MIS 2, controlled by sea level changes, monsoon oscillations as well as orographic effects (Ono et al., 2005; Sawagaki et al., 2004). However, the impact of late Cenozoic climate on rates of erosion and mountain relief remains disputed (e.g., Champagnac et al. 2014). For example, Molnar and England (1990) suggested an increase in relief due to (tectonic) isostatic uplift in response to glacial erosion, which was later questioned by Whipple et al. (1999). More recently, Herman et al. (2013) showed that glaciers played an important role in eroding landscapes at all latitudes leading to an

* Corresponding author.
E-mail address: melanie.bartz@unil.ch (M. Bartz).

https://doi.org/10.1016/j.epsl.2024.118830
Received 26 October 2023; Received in revised form 27 May 2024; Accepted 2 June 2024
Available online 21 August 2024

increase in sediment flux, which coincides with global cooling. Despite the important climatic setting of Japan, the impact of Quaternary climate change on the development of mountain relief is only poorly known. This is mainly due to the difficulties of constraining rates of Earth surface processes over glacial-interglacial cycles given the young age and the small total denudation after the onset of the uplift of the Japanese Alps (Sueoka et al., 2016).

Low-temperature thermochronometry is a widely used method for studying changes in topography through the effect of erosion in mountainous regions (Reiners and Brandon, 2006; Wagner and Reimer, 1972). During the last decades, trapped charge dating systems with ultra-low closure temperatures of <100 °C have been developed (Grün et al., 1999; Herman et al., 2010) to study cooling histories of near-surface rocks and exhumation rates in orogens over the recent past (Grün et al., 1999; Guralnik et al., 2015; Herman et al., 2010; King et al., 2016b, 2020). Recently, King et al. (2020, 2022) showed the high potential of luminescence and electron spin resonance (ESR) thermochronometry for constraining rates of surface processes in the northern Japanese Alps over glacial-interglacial cycles. The authors reported on rapid exhumation in the Kurobegawa plutonic complex in the HMR (northern Japanese Alps) with peak erosion of ~10 mm/yr during late Quaternary glaciation. However, the local climatic and tectonic setting of the plutonic complexes in Kurobe are likely not equivalent to other localities in the HMR. For example, equilibrium line altitude (ELA) modelling showed that the Kurobegawa area has not been glaciated during the past 0.1 Myr, whereas higher elevation regions were glaciated (King et al., 2022).

The Tateyama mountains in the HMR, to the west of the Kurobegawa area (Fig. 1), preserve many glacial features thought to have formed during MIS2 and MIS3/4 (e.g., cirques filled with moraine and till

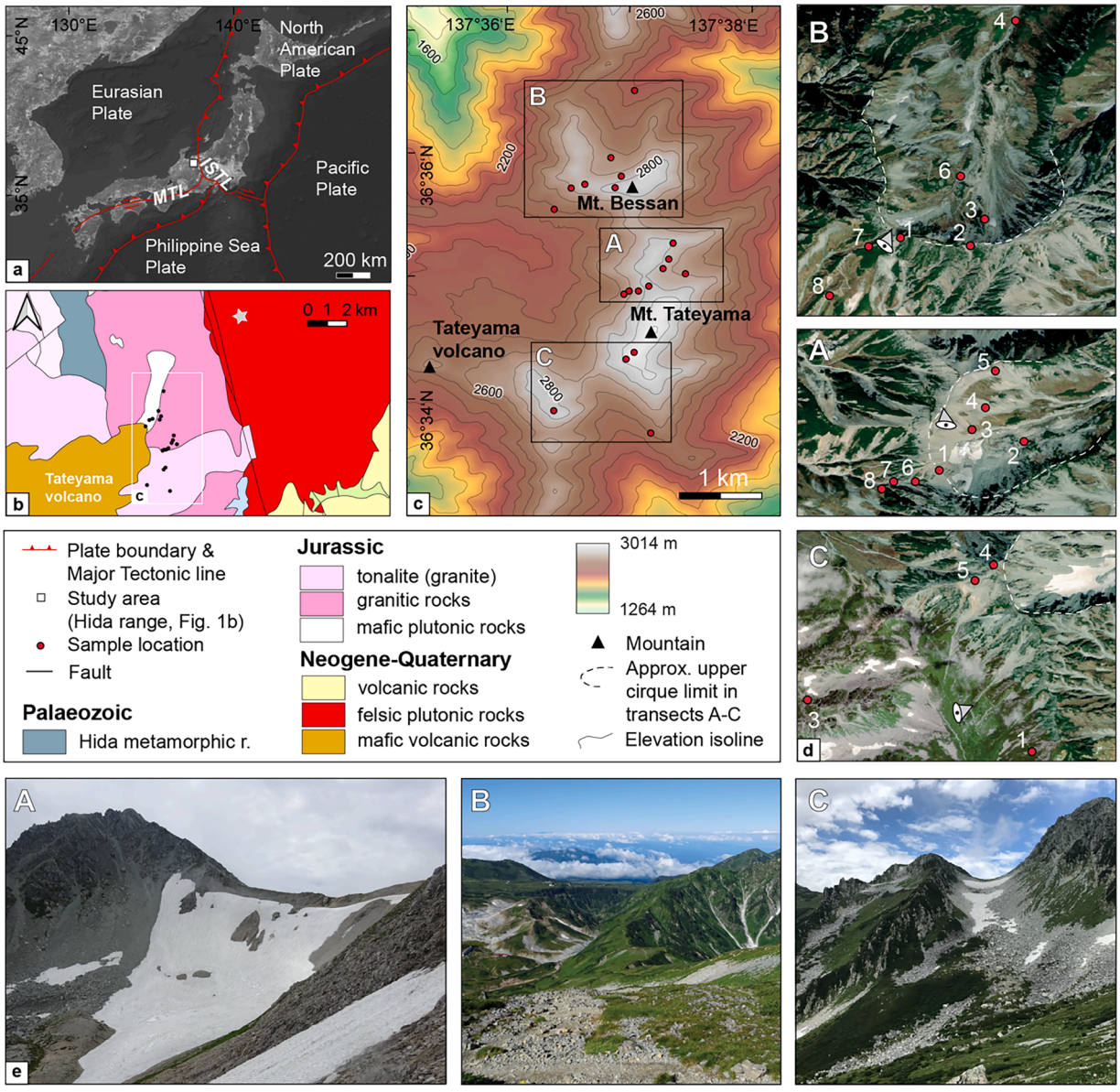

Fig. 1. Study area. a) Tectonic setting of the Japanese islands (map based on Bing Aerials). Tectonic fault lines are modified from Sueoka et al. (2016). MTL: Median Tectonic Line, ISTL: Itoigawa-Shizuoka Tectonic Line. The white rectangle highlights the study location in the Hida range; b) Geological map of the study area in the Hida range (modified from AIST, 2015 using QGIS v 3.10). The star marks the study area of King et al. (2022); c) Digital Elevation Model based on ASTER Global Digital Elevation Model 1 arc second, USGS, highlighting the three transects A, B, and C; d) Satellite images (Bing Aerials) of the three transects A-C with sample locations and IDs. The white dashed lines illustrate the approximate upper limit of the cirques (after Ono 1980); e) Exemplary imagery of the three transects (see "eyes" in d for picture locations). A – view to the cirque wall and the ridge top, B – view to the fluvially/periglacially characterised slope, and C – view to a glacially characterised slope (photographs by S. Sueoka, G. King, and Y. Kobayashi).

deposits; Ono, 1980; Ono et al., 2005) and have been regarded as type localities for glaciations in central Japan (Kawasumi, 2007). The Tateyama mountains are oriented N-S leading to characteristic geomorphological features on both sides of the ridge: glaciers and glacial erosion dominantly modified the landscapes on the eastern slopes, whilst the western slopes are predominantly characterised by periglacial and fluvial processes (Ono, 1980; Ono et al., 2005) due to an interaction of the westerlies and the winter monsoon with the orographic situation of the ridge (Kobayashi, 1958). Against this background, the Tateyama area is an excellent setting for studying changes in mountain denudation and relief under a changing climate during the Quaternary, the period when the Japanese Alps have been mainly formed (Harayama et al., 2003). We use ultra-low temperature thermochronometers using the luminescence of feldspar minerals and ESR of quartz minerals (King et al., 2020). Together with a thermal model (Biswas et al., 2018), this study will provide an improved understanding of the relief development of the HMR in response to distinct surface processes during the Quaternary period.

2. Study area

The Japanese islands are island arcs along the convergence zones between the Eurasian, North American, Pacific, and Philippine Sea plates (Taira, 2001). The present-day (Quaternary) tectonic motion is mainly controlled by the subduction of the Pacific and Philippine Sea plates at rates of 11 cm/yr and 4 cm/yr (Takahashi, 2006), respectively, causing an E-W compressional stress field around the Plio-Pleistocene boundary (Isozaki, 1996; Sato, 1994; Taira, 2001; Takahashi, 2006). In consequence, most of the topographic relief of the Japanese Alps, reaching an elevation up to 3000 m today, formed during the past few million years with accelerated uplift during the Quaternary (Ota et al., 2010; Sueoka et al., 2016; Yonekura et al., 2001). The HMR is the most extensive mountain range of the Japanese Alps, and it was uplifted from ~2.5 Ma until present, with two stages of uplift proposed by Oikawa (2003): the first stage is due to isostatic uplift related to magmatism, and the second stage is caused by E-W compression. Vertical crustal movement is estimated in the Tateyama area to up to 5 mm/yr based on GNSS data (Doke et al., 2008). The long-term exhumation history over 10^7–10^6 years timescales in the HMR has been inferred mainly from AFT and ZFT thermochronometry in the Kurobe area (Kurobegawa granite; see the comprehensive overview in Sueoka and Tagami 2019 and references therein). Based on terrestrial cosmogenic nuclides, Matsushi et al. (2014) reported on rates of denudation in the HMR between 0.2 and 7 mm/yr over 10^3–10^2 years, while King et al. (2022) showed rapid exhumation with rates of ~10 mm/yr within the past 65 ka in the Kurobe gorge (Fig. 1b) using ultra-low temperature thermochronometry. The authors reported peak erosion during cold climate periods linked to climatically controlled eustatic and surface process changes coupled with tectonics. Similarly high rates of exhumation were observed by Spencer et al. (2019) inferred from zircon and apatite (U-Th)/He thermochronological data. Whilst the exhumation history in the Quaternary plutons of the HMR is well studied, other areas such as the Tateyama region remain poorly investigated.

Our study area is in the Tateyama region of the HMR. The present climate in the northern Japanese Alps is influenced by the NW winter monsoon from Siberia over the Japan Sea (Estoque and Ninomiya, 1976; Ikeda et al., 2009; Watanabe, 1989). Heavy precipitation rates in the Tateyama mountains are estimated to be at least ~4800 mm/yr based on the sum of the maximum snow depth and summer precipitation (Fukui et al., 2021). The snow cover on Mt. Tateyama exhibits snow depths of 6–10 m persisting from November to July (Osada et al., 2004). The present ELA is estimated at 2970 m based on air temperature and precipitation data (Ono et al., 2003), which lies just below the peak of Mt. Tateyama (Fig. 1). Ono et al. (2004) reconstructed an MIS 2 ELA of ~2500 m, and an MIS 4/3 ELA of ~1900 m. Glacial modelling using the MIS 2 ELA indicates that ice was present in the Tateyama region during the Late Pleistocene (King et al., 2022), and was most likely more extensive during MIS 4/3 (Ono et al., 2005). Geomorphological evidence is found through for example cirques in the upper parts of the mountains, till and moraines up to an elevation of ~1900 m along NE- and E-facing slopes in the Tateyama mountains (Ono, 1980; Ono et al., 2005; Ono and Naruse, 1997; Sawagaki et al., 2004). Glacier extent in the Japanese Alps is controlled by monsoon changes, by zonal shifts in westerly circulation, and by sea-level fluctuations and related changes in sea-surface temperatures in the Japan Sea, which is the key moisture source (Ono et al., 2005). Presently few perennial snow patches mark the steep slopes of the Tateyama mountains, whilst it is still a matter of debate whether some perennial snow patches can rather be classified as glaciers (Arie et al., 2022).

In total 19 rock samples were collected along three transects (namely transects A, B, and C; Fig. 1) around Mt. Tateyama and Mt. Bessan (Fig. 1c) to explore the Pleistocene exhumation history of the Tateyama region of the HMR. The bedrock corresponds to the Jurassic Funatsu Granitic Rocks (Harayama et al., 2000) with emplacement ages ranging between ~200 and ~180 Ma based on whole rock mineral and isochron Rb-Sr and zircon U-Pb geochronology (e.g., Tanaka and Kagami 1987a, 1987b, Takehara and Horie 2019, Yamada et al. 2021). Samples were taken in the Kurobe (eastern slope) and Jyoganji (western slope) river catchments. Whereas the Tateyama volcano is located to the west of Mt. Tateyama (Fig. 1b), transects A and B contain massive granites (Fig. 1b). Transect C is characterised by massive granite, granodiorite and tonalite rocks (AIST, 2015). Specifically, samples were collected within cirque basins, at ridge tops, and on slopes that were affected by periglacial and slope processes to investigate exhumation in the area due to distinct surface processes (Fig. 1c).

3. Methods

3.1. Infrared stimulated luminescence (IRSL) and electron spin resonance (ESR) thermochronometry

Infrared stimulated luminescence (IRSL) of feldspar and ESR of quartz were used to determine the time since the mineral grains accumulated charge in the crystal lattice (i.e., electron traps and holes) due to the flux of environmental ionizing radiation since they cooled through the effective closure temperature. We used multiple trapped charge dating signals in feldspar (IR_{50}, IR_{100}, IR_{150}, IR_{225}) and quartz (Al and Ti centres), which all have different charge trapping and detrapping characteristics during rock cooling. Details of sample preparation as well as IRSL and ESR measurement apparatus and procedures can be found in supplementary material. Samples from all three transects were analysed using luminescence thermochronometry ($n = 19$), whilst only transect A was investigated using ESR thermochronometry ($n = 8$).

3.1.1. Kinetic models

We follow the approach of King et al. (2016c) for IRSL thermochronometry using the following differential equations to describe the change of trapped electrons with time:

$$\frac{d[\tilde{n}(r',E_b,t)]}{dt} = \frac{\dot{D}}{D_0}[1-\tilde{n}(r',E_b,t)] - s e^{-\frac{E_t-E_b}{k_B T}}[\tilde{n}(r',E_b,t)] - \tilde{s} e^{-\rho'^{-\frac{1}{3}} r'}[\tilde{n}(r',E_b,t)] \quad (1)$$

The first term on the right-hand side in Eq. (1) describes charge trapping where $\tilde{n}$ $(= n/N)$ is the trapped-charge population, $\dot{D}$ is the environmental dose rate (Gy/s), and D_0 is the characteristic saturation dose (Gy). The second term on the right-hand side describes thermal charge detrapping (i.e., thermal loss), which depends on the thermal kinetic parameters of the frequency factor s (s^{-1}), the activation energy E_t (eV), the band-tail state energy level E_b (eV), the Boltzmann constant k_B (eV/K), and the temperature T (K). The third term on the right-hand side in Eq. (1) describes athermal charge detrapping described following

the model of Huntley (2006), where $\tilde{s}$ is the athermal frequency factor (i.e., $3 \times 10^{15}\ s^{-1}$; Huntley, 2006), ρ' is the dimensionless density of the recombination centres and r' is the dimensionless distance between trapped electrons and their nearest neighbouring recombination centres. The total accumulation of charge with time, $\tilde{n}(t)$, is obtained by integrating $\tilde{n}(r',E_b,t)$ over the range of band-tail states, E_b, and an infinite range of dimensionless distances, r' with

$$\tilde{n}(t) = \int_{r'=0}^{\infty} \int_{E_{b=0}}^{E_t} p(r')P(E_b)\tilde{n}(r', E_b, t)dE_b dr' \tag{2}$$

where $p(r')$ is the probability density distribution of the nearest recombination centres (Huntley, 2006) and $P(E_b)$ is the probability density distribution of the band-tail states. Thermal detrapping is described here by using the band-tail states model (Li and Li, 2013) as implemented by King et al. (2016c) with

$$\frac{n(t)}{n(0)} = \varphi(t^*) \int_0^{E_t} P(E_b) e^{\left(-ste^{-\frac{E_t - E_b}{k_B T}}\right)} dE_b \tag{3}$$

where the probability of thermally evicting electrons into the band-tail states of energy in the range of $E_b + dE_b$, $P(E_b)dE_b$, is given by Poolton et al. (2009) and Li and Li (2013):

$$P(E_b)dE_b = Be^{\left(-\frac{E_b}{E_u}\right)} dE_b \tag{4}$$

where B and E_u are a pre-exponential multiplier and the width of the Urbach tail (eV), respectively.

For ESR thermochronometry, we follow the approach of King et al. (2020) which describes charge trapping and thermal charge detrapping on the right-hand side in Eq. (5):

$$\frac{d[\tilde{n}(E_a,t)]}{dt} = \frac{\dot{D}}{D_0}[1 - \tilde{n}(E_a,t)] - se^{-\frac{E_a}{k_B T}}[\tilde{n}(E_a,t)] \tag{5}$$

where

$$\tilde{n}(t) = \int_0^{\infty} P(E_a)\tilde{n}(E_a,t)dE_a \tag{6}$$

and

$$P(E_a) = \frac{1}{\sigma(E_t)\sqrt{2\pi}} \exp\left[-\frac{1}{2}\left(\frac{E_a - \mu(E_t)}{\sigma(E_t)}\right)^2\right] \tag{7}$$

Similar to IRSL thermochronometry, $\tilde{n}$ $(=n/N)$ in Eq. (5) describes how much signal has accumulated over time in the traps or holes dependent on the environmental dose rate ($\dot{D}$), the characteristic saturation dose (D_0), and the thermal history. We describe the thermal detrapping with a model that uses a Gaussian distribution of activation energies, $\sigma(E_t)$, around the trap depth $\mu(E_t)$ (eV) (Lambert, 2018; Faershtein et al., 2018) by the activation energy E_a (eV), and $P(E_a)$, which is the probability of thermally evicting electrons (or holes) from the trap (Eq. (7)).

3.1.2. Prediction of cooling histories

We follow the approach of King et al. (2016c) for the prediction of cooling histories. To derive cooling histories from the measured trapped-charge population of each of the samples, $\tilde{n}$, 10,000 random time-temperature (t-T) paths were generated, and a modelled $\tilde{n}_{mod}$ value computed for each of them by solving the differential Eqs. (1) and (5) using the sample specific kinetic parameters for feldspar IRSL and quartz ESR, respectively. Here, the cooling histories were constrained to cool monotonically between 200 °C and 5 ± 5 °C over 2 Ma. For each t-T path, we calculated a misfit between the final inverted trapped-charge population, $\tilde{n}_{mod}$, and the natural trapped-charge population, $\tilde{n}$, with an associated likelihood L:

$$M = \Sigma_1^m \left(0.5\ \frac{\tilde{n}}{\sigma}\ \left(\log\left(\frac{\tilde{n}}{\tilde{n}_{mod}}\right)\right)\right)^2 \tag{8}$$

$$L = \exp(-M) \tag{9}$$

where M is the misfit for m datasets and σ is the uncertainty. Cooling histories were accepted or rejected by contrasting L with a random number between 0 and 1 (Tarantola, 2005). The accepted cooling histories are then combined to construct a probability density function of time-temperature histories. This was done by summing the number of paths going through each cell of a 50-interval grid (i.e., time-temperature axis).

3.2. Prediction of exhumation paths

Exhumation histories were inferred by using the one-dimensional thermal kinematic model of Biswas et al. (2018). First, we generated 12,000 exhumation paths (i.e., time-depth, t-Z, paths) with monotonically decreasing depth up to 15 km over 5 Ma using a Monte Carlo (MC) approach. $\tilde{n}_{mod}$ values were then predicted for each t-Z path by solving the 1D-heat transfer equation:

$$\frac{\partial T}{\partial t} = \kappa\ \frac{d^2T}{dz^2} + \dot{e}\frac{dT}{dz} \tag{10}$$

where κ is the thermal diffusivity (30 km^2/Myr), T is the temperature, z is the depth (km), and $\dot{e}$ is the exhumation rate, which corresponds to the time derivate of t-Z. The number of steps in each exhumation history is random, and the MC search enables the full time-depth field to be explored. The model surface temperature of the present rocks was 5 ± 5 °C. We used an initial geothermal gradient of 30 °C/km and assumed flux boundary conditions at the model base (i.e., maximum depth). The geothermal gradient in the shallower crust (<2 km) influencing the trapped-charge dating signals will increase with time because of the exhumation rate history defined by the random path (i.e., due to heat advection caused by erosion). Therefore, we chose to truncate our data with a maximum geothermal gradient of 100 °C/km to avoid unrealistically high present-day near-surface geothermal gradients (>100 °C/km) and to allow geothermal gradients that are higher than 30 °C/km due to high-temperature volcanic gases in the hydrothermal system of the Jigokudani Valley, ~3 km to the west of transect A (Seki et al., 2015), and also to account for the shallow felsic magma reservoir underneath the Tateyama mountains (Matsubara et al., 2000). The best paths were then selected by calculating a misfit value with associated likelihood using Eqs. (8) and (9). An arbitrary uncertainty on $\tilde{n}_{mod}$ of 10% was assumed. The accepted t-Z paths were then used to construct a probability density function of exhumation in time (5–0 Myr) and depth (15–0 km). Finally, the derivative of the median and confidence intervals of the probability density function were used to calculate time-dependent exhumation rates.

4. Results

4.2. IRSL signal properties of feldspar

All analysed aliquots (n = 3 for each sample) fulfilled the standard SAR rejection criteria for recuperation (<5%), recycling ratio (<10%) and maximum test dose error (<10%). SAR dose response curve (DRC) fitting was performed using the single saturating exponential function resulting in mostly very good fit with adjusted r^2 values >0.97 (Tab. S1). Laboratory residual doses were on average ~2 Gy (IR_{50}), ~5 Gy (IR_{100}), ~7 Gy (IR_{150}), and ~12 Gy (IR_{225}). Dose recovery ratios were generally

low for most of the samples (Table S1). E_t values ranged from 1.44 eV to 1.86 eV between accepted samples and signals (Table S2). Anomalous fading rates ranged for the IR_{50} signals from 2.7 to 11.6% decade^{-1} showing the highest rates of the four IRSL signals. Whilst the IR_{225} signals of some samples were in the range of 2.3% decade^{-1}, the majority of IR_{225} signals yielded fading rates <1% decade^{-1} (Table S2). Fading data of samples A06-IRSL, B04-IRSL, B06-IRSL, and IR_{100} - IR_{225} signals of all samples from transect C were poor (i.e., scattered data points, poor fits) (Figs. S1–S10). According to the plot of $(n/N)_{ss}$ against $(n/N)_{nat}$, most accepted IRSL signals were in athermal field saturation, except for the signals of sample A07-IRSL (Fig. S11). Given the underestimated dose recovery results, n/N values might also be underestimated. Therefore, resulting cooling and exhumation rates might not be reliable. Minimum ages of accepted signals were ~51–207 ka, ~91–480 ka, and ~199–297 ka for samples from transects A, B, and C, respectively, derived from two times the characteristic saturation dose (D_0) for all IRSL signals (IR_{50}-IR_{225}) (Table S2), i.e. equivalent to $0.86*(n/N)_{ss}$. We excluded IR signals from samples with poor laboratory constraints (Table S2) and used only IR signals which fulfilled our quality control criteria (supplementary material section 1.5 and Tab. S2) for maximum exhumation rates modelling (assuming IRSL signals of $0.86*(nN)_{ss}$). However, these IRSL signals were not used to constrain an age-elevation relationship as the natural signals were saturated (Fig. S11).

4.3. ESR thermochronometry

4.3.1. ESR signal properties of quartz

ESR intensities of the Al and Ti signals were generally strong for all Tateyama samples (Fig. S12). Natural ESR intensities (with varying preheat temperatures) yielded a plateau between 20 °C and 160 °C for the Al centre and 20 °C and 180 °C for the Ti centre (Fig. S13a). Measured DRC without preheating and using preheat temperatures of 160 °C and 180 °C resulted in lower ESR intensities at higher doses, whilst the DRC shape did not change (Fig. S13b). Final D_e values were within error for the Ti centre, whilst the Al centre resulted in higher D_e values when using preheat temperatures higher than 160 °C (Fig. S13c). Thus, we chose a preheat temperature of 160 °C for further measurements. The Al centre yielded similar dose response curve shape between the single-aliquot additive dose (SAAD) and single-aliquot regenerative dose (SAR) methods (Fig. S14a) and using a single saturating exponential function, D_e values were 1529±256 Gy and 1599±149 Gy, respectively, indicating no significant sensitivity change due to the annealing step of the SAR protocol. In addition, sliding the SAAD additive dose points (i.e., additive dose plus regenerative D_e, Fig. S14) onto the SAR DRC suggested no sensitivity change as both curves were consistent. The comparison between the Ti SAAD and SAR DRC resulted in insignificant differences in the low dose region. The slight mismatch in the high dose region is due to the dose response curve approaching saturation and is

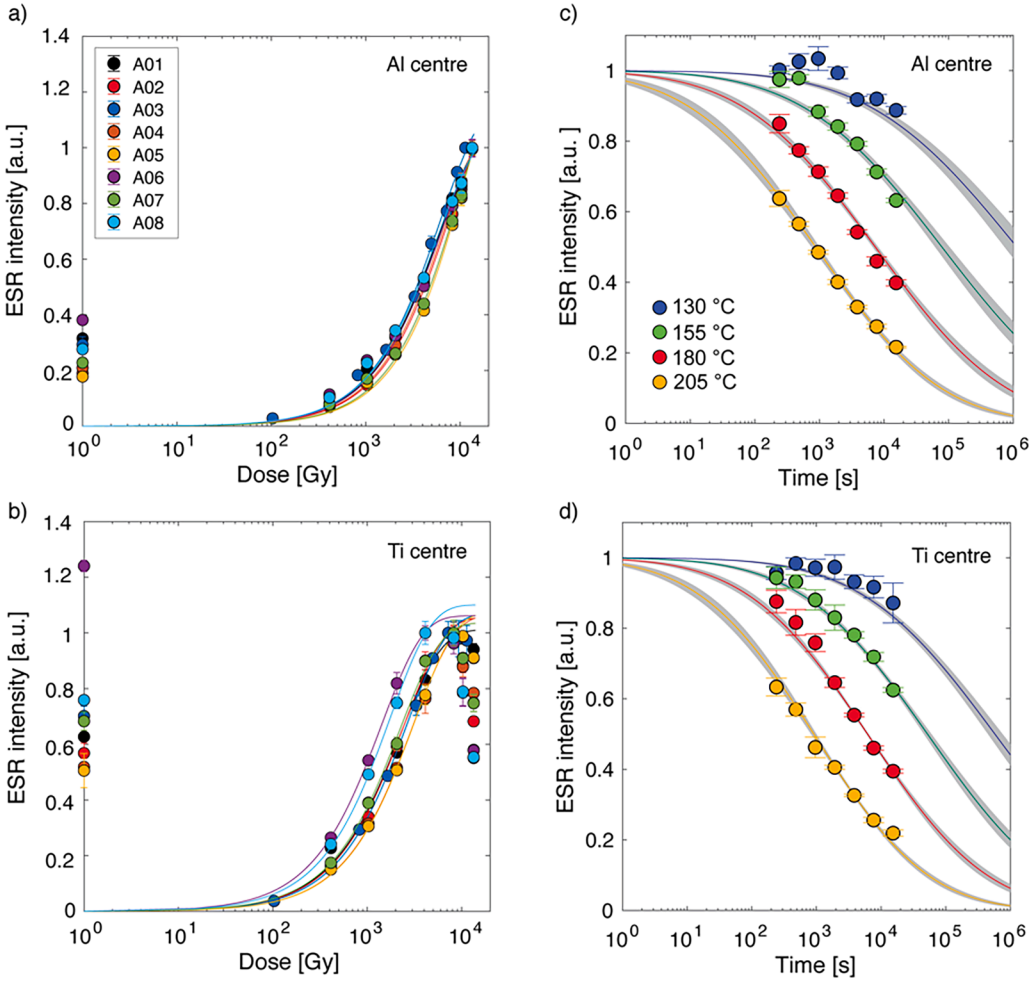

Fig. 2. ESR signal trapping and detrapping. a, b) Dose response curves (DRCs) of the Al and Ti centres for all ESR samples normalised to the maximum ESR intensity (I_{max}). DRCs were best fitted with a single saturating exponential function without data weighting. Ti centre DRCs were fitted until I_{max}. c, d) Exemplary ESR isothermal decay data of sample A07. Isothermal decay data were best fitted with a multiple 1st-order kinetic model assuming a Gaussian distribution of trap depths (i.e., Lambert, 2018, King et al. 2020). Data fitting was performed using data weighted by the inverse of the squared errors (i.e., 1-sigma standard deviation from the three rotations). All dose response and isothermal decay data are illustrated in Figs. S15 and S16.

Table 1
ESR data of the Al and Ti centres including kinetic parameters, D_e values, and ages. Maximum ages (Age_{max}) are based on $2*D_0$ values.

Sample-ID	Lat (N) (deg.)	Lon (E) (deg.)	Elev. (m)	μ(Et) (eV)	$\log_{10}$ (s) (s^{-1})	σ(Et) (eV)	D_0 (Gy)	n/N	$\dot{D}$ (Gy ka^{-1})	D_e (Gy)	Age (ka)	Age_{max} (ka)
A01-Al	36.58205	137.6194	2822	1.40±0.06	11.86±0.62	0.11±0.00	6114±350	0.28±0.01	4.45±0.46	2047±49	460±48	2747
A02-Al	36.58375	137.6244	2676	1.67±0.13	14.51±1.44	0.11±0.01	7709±463	0.16±0.00	2.03±0.16	1345±29	662±55	7591
A03-Al	36.58444	137.6214	2729	1.45±0.06	12.40±0.63	0.11±0.01	5691±401	0.26±0.01	4.52±0.44	1734±44	384±39	2520
A04-Al	36.58573	137.6221	2749	1.55±0.05	13.55±0.51	0.10±0.00	7208±351	0.18±0.01	4.38±0.43	1419±26	324±33	3293
A05-Al	36.58789	137.6227	2782	1.55±0.04	13.73±0.42	0.10±0.00	11,030±965	0.13±0.00	3.92±0.37	1509±37	386±38	5635
A06-Al	36.58139	137.6180	2731	1.93±0.06	16.68±0.66	0.16±0.01	6014±521	0.35±0.02	4.70±0.50	2600±95	554±63	2561
A07-Al	36.58139	137.6168	2665	1.59±0.06	13.56±0.68	0.14±0.01	9716±814	0.17±0.01	2.69±0.22	1859±48	692±60	7237
A08-Al	36.58096	137.6161	2633	1.50±0.08	12.37±0.81	0.15±0.01	5434±342	0.26±0.01	1.89±0.16	1649±46	878±77	5787
A01-Ti	36.58205	137.6194	2822	1.40±0.12	11.54±1.31	0.15±0.01	2256±140	0.62±0.04	4.45±0.46	2170±85	487±53	1014
A02-Ti	36.58375	137.6244	2676	1.42±0.06	11.96±0.68	0.11±0.01	2420±94	0.54±0.03	2.03±0.16	1860±48	916±77	2383
A03-Ti	36.58444	137.6214	2729	1.57±0.12	13.36±1.25	0.15±0.01	2560±91	0.66±0.05	4.52±0.44	2766±52	612±61	1133
A04-Ti	36.58573	137.6221	2749	1.56±0.16	13.24±1.73	0.13±0.01	3051±127	0.49±0.03	4.38±0.43	2035±54	465±48	1394
A05-Ti	36.58789	137.6227	2782	1.84±0.16	16.54±1.75	0.19±0.01	3088±101	0.48±0.04	3.92±0.37	1992±40	509±49	1577
A06-Ti	36.58139	137.6180	2731	1.78±0.11	15.27±1.16	0.13±0.01	1356±56	1.18±0.06	4.70±0.50	–	–	578
A07-Ti	36.58139	137.6168	2665	1.43±0.04	11.88±0.42	0.12±0.00	2214±103	0.66±0.04	2.69±0.22	2383±74	887±79	1649
A08-Ti	36.58096	137.6161	2633	2.17±0.17	19.83±1.85	0.15±0.01	1617±69	0.72±0.03	1.89±0.16	2040±64	1086±97	1722

not caused by sensitivity change (Fig. S14b). Moreover, recycling ratios within 5–15% of unity for both ESR signals (Table S3) of most samples indicate no sensitivity change.

Measurements of the trapped-charge population of the Al and Ti centres yielded similar DRC shapes between samples (Figs. 2a, b, S15, S16). ESR signal growth is best described by a single saturating exponential function with excellent goodness-of-fit with adj. r^2 values of >0.98 (Table S3). Dose response curves of the Ti centre signals saturate at ~6 kGy and yielded a non-monotonic behaviour at high doses (i.e., decreasing ESR intensities, Fig. 2b). The Al centre showed higher saturation levels >12 kGy. D_0 values ranged between 5.4 and 11.0 kGy for the Al centre and 1.4 and 3.1 kGy for the Ti centre, whilst final D_e values ranged between 1.4 and 2.6 kGy (Al centre) and 1.9 and 2.8 kGy (Ti centre). Sample A06-Ti had already reached signal saturation. Whilst sample A01 showed Al and Ti centre D_e values matching each other, Al centre D_e values were lower for the other samples compared to their Ti centre equivalents (Table 1).

Isothermal decay data were best fitted with a multiple 1st-order kinetic model assuming a Gaussian distribution of trap depths (i.e., Lambert, 2018, King et al. 2020). The goodness-of-fit is overall good with adj. r^2 values >0.97 for both ESR signals, except for A04-Ti with an adj. r^2 value of 0.96 (Table S3). Thermal stabilities of the Al and Ti centre signals generally agree with previous observations by King et al. (2020) showing lower stability for the Al centre (Fig. 2c,d). Al centre activation energies μ(E_t) ranged from 1.40 to 1.67 eV, and frequency factors $\log_{10}$(s) ranged from 11.86 to 14.51 s^{-1} for all samples, except for sample A06-Al which has μ(E_t) of 1.93±0.06 eV and a frequency factor $\log_{10}$(s) of 16.68±0.66 s^{-1} (Table 1). The Ti centre showed larger variations with activation energies ranging between 1.40 and 2.17 eV, frequency factors between 11.54 and 19.83 s^{-1}, and $\sigma(E_t)$ values between 0.11 and 0.15 eV (Table 1). We simulated the isothermal decay of the different samples for isothermal conditions of 20 °C using the experimentally constrained kinetic parameters (Table 1) to evaluate the lifetime of the ESR signals (Fig. S17). As the ESR signals presented here are not simple first-order concepts, the estimated lifetimes are approximations. Both signals are sufficiently stable for dating over Quaternary timescales with approximate lifetimes on the order of 10^8–10^{16} years (Fig. S18). The simulations showed generally lower thermal stability for the Al centre compared to the Ti signals, with a slight trend towards lower stability of the Al centre at higher elevations. A moderate correlation between the Al signal lifetime and elevation has also been observed by multivariate statistical analysis, which is not the case for the Ti signal (Fig. S19).

4.3.2. ESR ages and their age-elevation relationship (AER)

Thermochronometric ages can be constrained for the eight ESR samples of transect A, except for the Ti centre of sample A06. The latter sample resulted in a minimum ESR age of ~0.6 Ma (i.e., $2*D_0$) (Table 1). The apparent ages of the Al and Ti centres range between 0.3–0.9 Ma and 0.5–1.1 Ma, respectively (Table 1). The thermal stability of the Al centre is lower than that of the Ti centre, which is evident in lower Al ages compared to the Ti ages (Fig. 3). The age-elevation relationship (AER) shows a slightly positive trend in the Al ages at elevations of >2750 m (i.e. between A04, A05 and A01) and then a first-order negative trend at lower elevations. Both signals show a more crescent-like shape in their age-elevation relationship.

4.3.3. Rock cooling histories

The ESR data of transect A were inverted into cooling histories, whilst no IRSL data were used in the inversions due to signal saturation. We first inverted the ESR data separately and then together. Predicted ESR signals showed very good agreement with the measured Al and Ti signals, except for the Ti signals of samples A02 and A07 where slightly higher natural n/N values were observed compared to modelled values (Fig. S20). Inverse modelling revealed rock cooling rates on the order of ~23–85 °C/Myr for the Al centre, and slower cooling rates of 12–60 °C/

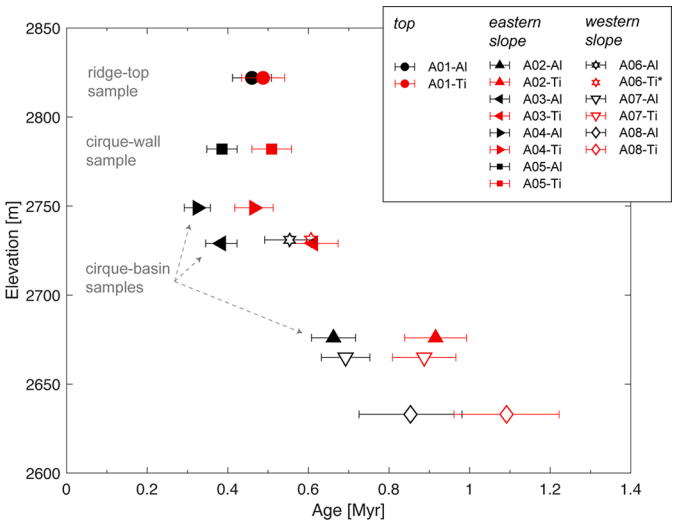

Fig. 3. Age vs. elevation of ESR Al (black) and Ti (red) signals of samples from transect A. *Ti centre signal of sample A06 is saturated, the two times D_0 age is shown.

Myr for the Ti centre (Table S4). The Ti centre of samples A02 and A07 yielded very slow cooling <20 °C/Myr (Fig. S21, Table S4), which might also be an effect of the poor fitting results between nN_{mod} and nN_{obs} (Fig. S20). The disagreement between our laboratory and modelling results for the Ti signals of samples A02 and A07 leads to large uncertainties for further interpretations. When inverting both ESR signals together, rock cooling rates between ~19 and ~53 °C could be observed over the past 1 Myr (Fig. S21, Table S4). For samples A02 and A07, only the Al centre cooling rates were considered for further geomorphological interpretations, whilst combined Al/Ti-cooling rates were used for the other samples. Closure temperatures of the Al and Ti centres are presented in Fig. S22 and show a correlation of both ESR signals with their thermal kinetic parameters and slightly with elevation (Fig. S22).

4.4. Exhumation history of the Tateyama mountains

In order to constrain a maximum exhumation rate from the saturated IRSL data, we modelled IRSL signals assuming n/N values close to saturation (i.e., 86% of $(n/N)_{ss}$) from accepted samples with appropriate IRSL signal properties only (Table S1, Fig. S23). We excluded samples with poor misfit values (Figs. S23 and 24). Inverse modelling revealed maximum average exhumation rates of ~1–1.5 mm/yr over the past 0.1 Myr (Figs. 4, S24). Most samples show peak maximum exhumation rates between ~0.1 and 0.2 Ma, which might be biased by the apparent ages in that time range (Fig. 4). In general, these maximum rates should be taken as an approximation rather than precise rates given the high uncertainty in the modelling results of the IRSL signals (Figs. S23 and S24). In contrast, natural ESR signals could be used to derive exhumation rates for samples from transect A over 10^6 years timescales (Figs. S25 and S26). Given the poor Ti fitting results for samples A02 and A07 (i.e., low number of accepted paths; Fig. S25), we excluded the Ti centre data of these samples from further exhumation rate analyses. Inverse modelling of the Al centre alone of the two samples yielded accepted paths of 994 and 1103, and less uncertainty in the resulting exhumation rates.

In order to compare the ESR exhumation rates with the maximum IRSL exhumation rates, we also averaged the ESR exhumation rates over the past 0.1 Myr (Fig. 5). These rates are significantly lower than 1 mm/yr and more on the order of 0.5 mm/yr, which is in agreement with the maximum IRSL exhumation rates over the past 0.1 Myr (Fig. 4). When considering the sample specific apparent ages, samples A01-Al-Ti and A08-Al-Ti yielded the lowest exhumation rates of ~0.25 mm/yr without remarkable changes over the past 0.5 and 1 Myr, respectively (Fig. 5).

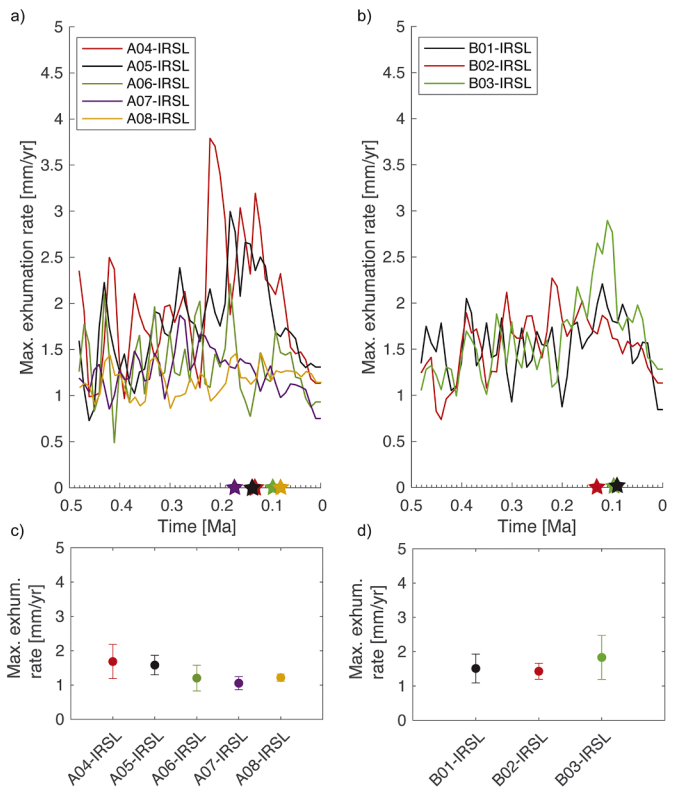

Fig. 4. Maximum IRSL exhumation rates for samples from transect A (a, c) and transect B (b, d). a and b) Median exhumation rates calculated from inversion of IRSL data using a 1D thermal model following Biswas et al. (2018). As the natural IRSL signals are saturated, 86% of $(n/N)_{ss}$ was used to invert maximum exhumation rates from the IRSL data. The stars mark the $2*D_0$ ages of the accepted IR_{225} signals. Note that the median exhumation rates were smoothed using a moving average; c and d) Exhumation rates and 1-sigma standard deviation averaged over the past 0.1 Myr.

Samples from the Kuranosuke cirque (A02–05) yielded average rates of ~0.5 mm/yr with slightly higher rates before 0.5 Myr for sample A02 (Fig. 5b). Slightly higher average rates of ~0.8 mm/yr were also observed for sample A07 from 0.75 to 0.5 Myr before decreasing to 0.4 mm/yr over the past 0.5 Myr (Fig. 5b). The highest rates were observed for sample A06 of ~1.1 mm/yr over the past 0.5 Myr before decreasing to ~0.7 mm/yr within the past 0.1 Myr (Fig. 5a). However, uncertainties of exhumation rates are higher for sample A06. In general, the latter sample seems to be an outlier of the data set which differs in terms of its kinetic parameters (Table 1) and its thermal history compared to the other samples (Figs. S21 and S22).

5. Discussion

Luminescence and ESR systems belong to the group of leaky and saturating thermochronometers, which challenges the evaluation of the closure isotherm that the minerals have passed since the onset of signal growth (Guralnik et al., 2013). The low closure temperatures of the ESR signals (Fig. S22) suggest isotherms at depths within 1–2 km in the shallow crust, which follow the topography (Braun, 2002; King et al., 2016a). This makes the ESR thermochronometers very sensitive to changes in surface topography as predicted by Braun (2002) for low-temperature thermochronometers based on a 3D-thermal kinematic model. Whilst Tateyama luminescence samples have reached their upper dating limits, yielding only minimum cooling ages of between 0.05 Ma and 0.48 Ma (Table S2), ESR thermochronometric ages of samples from transect A date back to ~0.3–1.1 Ma providing thus insights into landscape evolution during the Pleistocene.

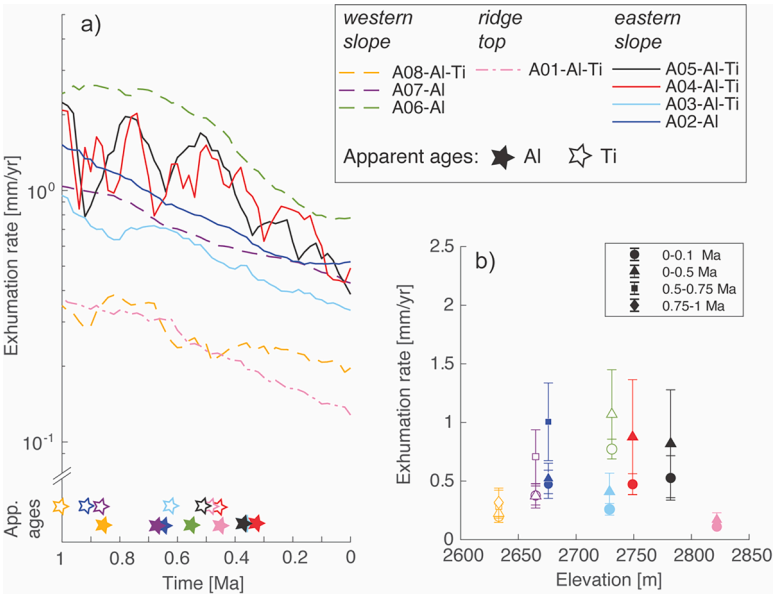

Fig. 5. Exhumation rates calculated from inversion of ESR data using a 1D thermal model following Biswas et al. (2018). a) Median exhumation rates shown over 1 Myr (see also Fig. S26). Samples collected from the top of the ridge (solid-dotted line), the Kuranosuke cirque (solid lines), and samples that are affected by fluvial and/or periglacial processes (dashed lines) are shown from transect A. Note that the median exhumation rates were smoothed using a moving average; b) average exhumation rates over the past 0.1 Myr (circles, for comparison with IRSL max. exhumation rates), 0–0.5 Ma (triangles), 0.5–0.75 Ma (squares), and over 0.75–1 Ma (diamonds). Average exhumation rates were calculated over timescales below or equal to the sample-specific apparent ages (stars in Fig. 5a). Filled symbols correspond to the top and eastern slope (cirque) samples, whilst the unfilled symbols belong to western slope samples. No curve smoothing was used before averaging exhumation rates over the specific time periods. The errors correspond to 1-sigma standard deviations of the averaged medians.

The distribution of ESR ages with elevation from transect A (Fig. 3) shows a crescent-like pattern for both Al and Ti centres. Whilst the youngest ESR ages (~0.3–0.5 Ma) are found at the cirque wall and at the ridge top, slope samples yielded systematically older ESR ages (~0.5–1.1 Ma) towards lower elevations (Fig. 3). Braun (2002) predicted that a reduction in surface relief would result in a negative AER, as observed for the ESR ages presented here (Fig. 3). Glacial erosion has been argued to result in relief reduction associated with concentration of erosion at higher altitudes, reduction of fluvial erosion downstream of the glaciers, and a possible acceleration of summit-lowering rates in the near-glacial environment (Whipple et al., 1999) and cirques in the Tateyama region indicate intense glacial erosion at and above the glacier's long-term ELA at a local scale. Herman et al. (2011) found a bimodal distribution of glacial erosion with peak erosion around the ELA and enhanced erosion at lower altitudes based on a glacial erosion model. Such a distribution of glacial erosion rates is documented in Norway (Steer et al., 2012) and the European Alps (Sternai et al., 2013).

Although glaciation in the HMR has been locally intense, it has been however much less extensive compared to Norway or the European Alps. For example, based on terminal moraines in the Kuranosuke cirque, a downstream extension during the LGM of ~1.2 km has been estimated (Watanabe, 1989). Thus, small glacier size and limited extent in the HMR likely led to limited carving of troughs of channeled ice in the downslope direction, which are rather affected by fluvial processes. In this study, although modelled exhumation rates have high uncertainties (Figs. 5b and S24), there is a trend towards slightly higher glacial erosion rates compared to rates from the western slope over the past 0.5 Myr (Fig. 5b). These results are consistent with the rock cooling rates for samples from the Kuranosuke cirque (Fig. S21), which show cooling from ~45–70 °C over the past 1 Myr, whereas samples from outside of the cirque basin exhibit slower rates of rock cooling (Table S4). Thus, our data suggest that cirque relief developed during the past 1 Myr. Similar observations have been reported using (U/Th)He and $^{4}He/^{3}He$ dating of apatite for the glacial landscape of Fiordland, New Zealand, due to headward propagation of glacial erosion (Shuster et al., 2011). However, our study area is more localized than the latter study, thus giving insights into relief evolution at the scale of an individual cirque-basin rather than at the scale of the mountain range. Whilst samples from the Kuranosuke cirque reveal average rates of ~0.5–1 mm/yr, equating to at least ~250 m of exhumation over the past 0.5 Myr, the west-facing slope yielded exhumation rates of ~0.3 mm/yr, equating to ~150 m of exhumation over the past 0.5 Myr. Similar rates are observed for the period before 0.5 Ma for samples with higher apparent ages (Fig. 5), whilst differences for samples A02 and A07 can be related to uncertainties arising from the modelling of the Al centre only. Our data imply that more intense erosion has taken place in the cirque basin and when considering the exhumation rates of the cirque-basin samples, a very localized relief reduction is observed for the lower part of the cirque basin. Thus, the first-order negative trend of the AER can suggest a decrease in relief and incision of the glacial cirque throughout the late Quaternary (Fig. S27).

This hypothesis was further tested using Pecube (Braun et al., 2003, 2012) by modelling the ESR data of transect A using different topographic change scenarios (i.e., no change, increase and decrease of relief). The negative AER can be well predicted using Pecube (Fig. S28), although it has been shown that the negative trend is partly induced by the moderate correlation between thermal kinetic parameters and sample elevations (Figs. S19, S22). In contrast, different thermal sensitivities of the samples challenge the reproduction of the crescent-like shape of the AER. The Pecube modelling results are in general agreement with our 1D-modelling results in terms of cooling histories and exhumation rates; samples in the cirque basin must have experienced more recent cooling than the surroundings samples. However, inversion results from our Pecube modelling suggest that ESR data alone do not have sufficient resolution to constrain the topographic relief scenario, because of a trade-off between regional denudation rate and relief change (Fig. S29 and discussion). While a relief decrease scenario cannot be excluded, a higher temperature thermochronometer such as apatite (U-Th)/He may be required to add more constrains.

Samples near to and at the peak do not follow the negative AER, indicating that a potential relief reduction is very localized along the mountain slopes rather than at the peak. In contrast, using numerical

models, Tomkin and Braun (2002) predicted relief reduction through peak erosion, especially where glaciers are warm based. Warm-based glaciation seems likely for the northern Japanese Alps where a temperate climate has been estimated during the LGM around the ELA (Kobayashi, 1958) but the small size of the glaciers has likely limited peak erosion in the Tateyama mountains. This is also supported by the steady exhumation rates over the past 1 Myr of ~0.25 mm/yr observed at the ridge top (sample A01), which is the lowest rate along the sampling transect, and can be considered as the background erosion rate in the Tateyama region, demonstrating that the mountain peak is not affected by a relief reduction.

In general, successive migration of the ELA throughout the Quaternary in response to a changing climate likely affected the distribution of both glacial erosion and periglacial processes (Kobayashi, 1958). Changes in precipitation over the Pleistocene might have led to snow cover exceeding 6–10 m/yr (Osada et al., 2004), leading to enhanced erosion due to for example nivation (Ono, 1980), enhanced glaciation or periglacial weathering as reported from alpine glaciers in the Canadian Rockies (Sanders et al., 2012). This interplay of glacial and periglacial erosion may explain why the time-series of exhumation rates do not show a clear trend towards higher rates during glacial periods at ~65 ka and ~20 ka as observed from King et al. (2022) from Kurobe ~5 km to the NE of the Tateyama area (Fig. 1b). This likely reflects the relatively high-resolution dataset from that study, where it was possible to combine IRSL and ESR data from the same samples, as the IRSL ages were not already in field saturation. Furthermore, the authors reported exhumation rates up to one order of magnitude higher than in the Tateyama mountains. This difference in exhumation rates is likely due to the distinct lithologic-geomorphic coupling between phases of magmatism and surface processes (e.g. Ito et al. 2021) as has previously been identified elsewhere, such as at the Eastern Himalayan syntaxis (e.g., Zeitler et al. 2014).

Our samples were collected in the upper elevations of the Kurobe and Jyoganji catchments, two of the steepest rivers in Japan (Yoshimura et al., 2005). Erosion rates on the order of <1 mm/yr from the steep high-mountain environment of Tateyama are consistent with the basin-averaged erosion rates of Matsushi et al. (2014), who also reported on a decline of erosion rates for the steeper basins of the Takase and Ashima rivers in the HMR. Higher rates of erosion are expected further downstream where deeply incised fluvial valleys are formed as shown from the Kurobe gorge by King et al. (2022). Recent uplift rates in the Tateyama area are estimated to be ~5 mm/yr based on GNSS data (Doke et al., 2008), which are 5–10 times higher than the modelled exhumation rates at high altitudes in the Tateyama mountains (Fig. 5). Thus, we propose that the high-altitude mountain slopes of the Tateyama region experience cirque headwall retreat in combination with periglacial and slope processes, whilst the Tateyama mountains may still be developing given the imbalance between our estimated erosion rates and reported uplift rates.

6. Conclusion

Here we apply the recently established ESR-thermochronometry method to constrain the Quaternary exhumation history of a formerly glaciated landscape. ESR signals are sensitive to closure isotherms within 1–2 km of the surface, allowing the effect of changing surface processes on exhumation rates to be constrained. For the first time, we provide experimental data that show a negative AER as predicted by Braun (2002) for a localized reduction in relief within a cirque basin. Our data suggest that during the Quaternary the cirque slope of the Tateyama mountains experienced a very localized relief reduction in response to glacial and periglacial processes, whilst our data imply that the mountain peaks were not affected. This result shows that ESR thermochronometry can identify patterns of erosion due to distinct geomorphic processes over the recent past at a local scale. Thus, we propose that the highly active landscape in the Tateyama mountains is controlled by an interplay of distinct geomorphic features and Quaternary climate change.

CRediT authorship contribution statement

M. Bartz: Methodology, Validation, Writing – original draft, Writing – review & editing. **G.E. King:** Conceptualization, Methodology, Project administration, Funding acquisition, Writing – original draft, Investigation, Writing – review & editing. **M. Bernard:** Methodology, Validation, Writing – review & editing. **F. Herman:** Methodology, Validation, Writing – original draft, Investigation, Writing – review & editing. **X. Wen:** Methodology, Writing – review & editing. **S. Sueoka:** Writing – original draft, Investigation, Writing – review & editing. **S. Tsukamoto:** Methodology, Writing – original draft, Investigation, Writing – review & editing. **J. Braun:** Methodology. **T. Tagami:** Writing – original draft, Investigation, Writing – review & editing.

Declaration of competing interest

The authors declare that they have no known competing financial interests or personal relationships that could have appeared to influence the work reported in this paper.

Data availability

All data generated or analysed during this study are included in this manuscript or its supplementary material.

Acknowledgements

Sample collection and luminescence analyses were supported by the Swiss National Science Foundation (grant no. PZ00P2_167960). Further analyses were part of a project that has received funding from the European Research Council (ERC) under Horizon 2020 research and innovation programme (Grant agreement No. 851614) awarded to GEK. This work was supported by the Grant-in-Aid for Scientific Research on Innovative Areas (KAKENHI No. 26109002) from the Ministry of Education, Culture, Sports, Science and Technology (MEXT). The fieldwork was assisted by Cécile Gautheron, Guillaume Delpech, Floriane Ahadi (Université Paris), Stefan Schwartz (Université Grenoble Alpes), Thierry Coowar (University of Lausanne), Kotaro Fukui (Tateyama Caldera Sabo Museum), Tetsuya Komatsu, Shuji Terusawa (Japan Atomic Energy Agency), Shoma Fukuda, Takayuki Arai, Ai Shishikura, and Yumi Kobayashi (Kyoto University).

Supplementary materials

Supplementary material associated with this article can be found, in the online version, at doi:10.1016/j.epsl.2024.118830.

References

AIST, 2015. Seamless digital geological map of Japan 1: 200,000. May 29, 2015 version. Geological Survey of Japan. National Institute of Advanced Industrial Science and Technology. Geological Survey of Japan.

Arie, K., Narama, C., Yamamoto, R., Fukui, K., Iida, H., 2022. Characteristics of mountain glaciers in the northern Japanese Alps. Cryosphere 16, 1091–1106. https://doi.org/10.5194/tc-16-1091-2022.

Biswas, R.H., Herman, F., King, G.E., Braun, J., 2018. Thermoluminescence of feldspar as a multi-thermochronometer to constrain the temporal variation of rock exhumation in the recent past. Earth Planet. Sci. Lett. 495, 56–68. https://doi.org/10.1016/j.epsl.2018.04.030.

Braun, J., 2002. Quantifying the effect of recent relief changes on age–elevation relationships. Earth Planet. Sci. Lett. 200, 331–343. https://doi.org/10.1016/S0012-821X(02)00638-6.

Braun, J., 2003. Pecube: a new finite-element code to solve the 3D heat transport equation including the effects of a time-varying, finite amplitude surface topography. Comput. Geosci. 29, 787–794. https://doi.org/10.1016/S0098-3004(03)00052-9.

Braun, J., van der Beek, P., Valla, P., Robert, X., Herman, F., Glotzbach, C., Pedersen, V., Perry, C., Simon-Labric, T., Prigent, C., 2012. Quantifying rates of landscape evolution and tectonic processes by thermochronology and numerical modeling of crustal heat transport using PECUBE. Tectonophysics 524–525, 1–28. https://doi.org/10.1016/j.tecto.2011.12.035.

Champagnac, J.D., Valla, P.G., Herman, F., 2014. Late-Cenozoic relief evolution under evolving climate: a review. Tectonophysics 614, 44–65. https://doi.org/10.1016/j.tecto.2013.11.037.

Doke, R., Takeuchi, A., Yasue, K., Hatamoto, K., Matsu'ura, Y., 2008. Recent crustal movement inferred from GPS observation of Mt. Tateyama, Northern Alps, Central Japan. Bull. Earthq. Res. Inst. 83, 193–201. https://doi.org/10.15083/0000032452 (in Japanese with English abstract).

Estoque, M.A., Ninomiya, K., 1976. Numerical simulation of Japan Sea effect snowfall. Tellus 28, 243–253. https://doi.org/10.1111/j.2153-3490.1976.tb00672.x.

Faershtein, G., Guralnik, B., Lambert, R., Matmon, A., Porat, N., 2018. Investigating the thermal stability of TT-OSL main source trap. Radiat. Meas. 119, 102–111. https://doi.org/10.1016/j.radmeas.2018.09.010.

Fukui, K., Iida, H., Kosaka, T., 2021. Newly identifying active glaciers in the Northern Japanese Alps and their characteristics (English translation). Geograph. Rev. Jpn. Ser. B 94, 81–95. https://doi.org/10.4157/geogrevjapanb.94.81.

Grün, R., Tani, A., Gurbanov, A., Koshchug, D., Williams, I., Braun, J., 1999. A new method for the estimation of cooling and denudation rates using paramagnetic centers in quartz: a case study on the Eldzhurtinskiy Granite, Caucasus. J. Geophys. Res. Solid Earth 104, 17531–17549. https://doi.org/10.1029/1999JB900173.

Guralnik, B., Jain, M., Herman, F., Paris, R.B., Harrison, T.M., Murray, A.S., Valla, P.G., Rhodes, E.J., 2013. Effective closure temperature in leaky and/or saturating thermochronometers. Earth Planet. Sci. Lett. 384, 209–218. https://doi.org/10.1016/J.EPSL.2013.10.003.

Guralnik, B., Jain, M., Herman, F., Ankjærgaard, C., Murray, A.S., Valla, P.G., Preusser, F., King, G.E., Chen, R., Lowick, S.E., Kook, M., Rhodes, E.J., 2015. OSL-thermochronometry of feldspar from the KTB borehole, Germany. Earth Planet. Sci. Lett. 423, 232–243. https://doi.org/10.1016/j.epsl.2015.04.032.

Harayama, S., Takahashi, Y., Nakano, S., Kariya, Y.andKomazawa, M., 2000. Geology of the Tateyama district. With Geological Sheet Map at 1:50,000, Geol. Surv. Japan, 218. (in Japanese with English abstract).

Harayama, S., Ohyabu, K., Miyama, Y., Adachi, H., Shukuwa, R., 2003. Eastward tilting and uplifting after the late early pleistocene in the eastern-half area of the Hida Mountain Range (in Japanese with english abstract). Quat. Res. (Daiyonki Kenyu) 42, 127–140. https://doi.org/10.4116/jaqua.42.127.

Herman, F., Beaud, F., Champagnac, J.D., Lemieux, J.M., Sternai, P., 2011. Glacial hydrology and erosion patterns: a mechanism for carving glacial valleys. Earth Planet. Sci. Lett. 310, 498–508. https://doi.org/10.1016/j.epsl.2011.08.022.

Herman, F., Rhodes, E.J., Braun, J., Heiniger, L., 2010. Uniform erosion rates and relief amplitude during glacial cycles in the Southern Alps of New Zealand, as revealed from OSL-thermochronology. Earth Planet. Sci. Lett. 297, 183–189. https://doi.org/10.1016/j.epsl.2010.06.019.

Herman, F., Seward, D., Valla, P.G., Carter, A., Kohn, B., Willett, S.D., Ehlers, T.A., 2013. Worldwide acceleration of mountain erosion under a cooling climate. Nature 504, 423–426. https://doi.org/10.1038/nature12877.

Huntley, D.J., 2006. An explanation of the power-law decay of luminescence. J. Phys. Condens. Matter 18, 1359–1365. https://doi.org/10.1088/0953-8984/18/4/020.

Ikeda, S., Wakabayashi, R., Izumi, K., Kawashima, K., 2009. Study of snow climate in the Japanese Alps: comparison to snow climate in North America. Cold Reg. Sci. Technol. 59, 119–125. https://doi.org/10.1016/j.coldregions.2009.09.004.

Isozaki, Y., 1996. Anatomy and genesis of a subduction-related orogen: a new view of geotectonic subdivision and evolution of the Japanese Islands. Isl. Arc 5, 289–320. https://doi.org/10.1111/j.1440-1738.1996.tb00033.x.

Ito, H., Adachi, Y., Cambeses, A., Bea, F., Fukuyama, M., Fukuma, K., Yamada, R., Kubo, T., Takehara, M., Horie, K., 2021. The Quaternary Kurobegawa Granite: an example of a deeply dissected resurgent pluton. Sci. Rep. 11, 22059. https://doi.org/10.1038/s41598-021-01562-2.

Kawasumi, T., 2007. Timing of glacial advances and volcanic activities on Mt. Tateyama, Hida Range, Central Japan during the Late Stade of the Last Glacial Period. Quat. Res. (Daiyonki Kenkyu) 46, 37–46. https://doi.org/10.4116/jaqua.46.37.

King, G.E., Guralnik, B., Valla, P.G., Herman, F., 2016a. Trapped-charge thermochronometry and thermometry: a status review. Chem. Geol. 446, 3–17. https://doi.org/10.1016/J.CHEMGEO.2016.08.023.

King, G.E., Herman, F., Guralnik, B., 2016b. Northward migration of the eastern Himalayan syntaxis revealed by OSL thermochronometry. Science 353, 800–804. https://doi.org/10.1126/science.aaf2637 (1979).

King, G.E., Herman, F., Lambert, R., Valla, P.G., Guralnik, B., 2016c. Multi-OSL-thermochronometry of feldspar. Quat. Geochronol. 33, 76–87. https://doi.org/10.1016/j.quageo.2016.01.004.

King, G.E., Tsukamoto, S., Herman, F., Biswas, R.H., Sueoka, S., Tagami, T., 2020. Electron spin resonance (ESR) thermochronometry of the Hida range of the Japanese Alps: validation and future potential. Geochronology 2, 1–15. https://doi.org/10.5194/gchron-2-1-2020.

King, G.E., Ahadi, F., Sueoka, S., Herman, F., Anderson, L., Gautheron, C., Tsukamoto, S., Stalder, N., Biswas, R., Fox, M., Delpech, G., Schwartz, S., Tagami, T., 2022. Eustatic change modulates exhumation in the Japanese Alps. Geology. https://doi.org/10.1130/G50599.1.

Kobayashi, K., 1958. Quaternary glaciation of the Japan Alps. J. Fac. Lib. Arts Sci. 13–67.

Lambert, R., 2018. Investigating thermal decay in K-feldspar for the application of IRSL thermochronometry on the Mont Blanc massif. Université de Lausanne, Lausanne.

Li, B., Li, S.H., 2013. The effect of band-tail states on the thermal stability of the infrared stimulated luminescence from K-feldspar. J. Lumin. 136, 5–10. https://doi.org/10.1016/j.jlumin.2012.08.043.

Matsubara, M., Hirata, N., Sakai, S., Kawasaki, I., 2000. A low velocity zone beneath the Hida Mountains derived from dense array observation and tomographic method. Earth Planets Space 52, 143–154. https://doi.org/10.1186/BF03351623.

Matsushi, Y., Matsuzaki, H., Chigira, M., 2014. Determining long-term sediment yield from mountainous watersheds by terrestrial cosmogenic nuclides (in Japanese with English abstract). J. Jpn. Soc. Eng. Geol. 54, 272–280. https://doi.org/10.5110/jjseg.54.272.

Molnar, P., England, P., 1990. Late Cenozoic uplift of mountain ranges and global climate change: chicken or egg? Nature 346, 29–34. https://doi.org/10.1038/346029a0.

Oikawa, T., 2003. The spatial and temporal relation- ship between uplifting and magmatism in the Hida mountain range, central Japan. Quat. Res.(Daiyonki Kenkyu) 42, 141–156. https://doi.org/10.4116/jaqua.42.141 (in Japanese with English abstract).

Ono, Y., 1980. Glacial and periglacial geomorphology in Japan. Prog. Phys. Geogr. Earth Environ. 4, 149–160. https://doi.org/10.1177/030913338000400201.

Ono, Y., Aoki, T., Hasegawa, H., Dali, L., 2005. Mountain glaciation in Japan and Taiwan at the global Last Glacial Maximum. Quat. Int. 138–139, 79–92. https://doi.org/10.1016/j.quaint.2005.02.007.

Ono, Y., Naruse, T., 1997. Snowline elevation and eolian dust flux in the Japanese Islands during Isotope Stages 2 and 4. Quat. Int. 37, 45–54. https://doi.org/10.1016/1040-6182(96)00003-1.

Ono, Y., Shiraiwa, T., Liu, D., 2003. Present and last-glacial equilibrium line altitudes (ELAs) in the Japanese high mountains. Zeitschrift fur Geomorphologie, Neue Folge Supplement 130, 217–236.

Ono, Y., Shulmeister, J., Lehmkuhl, F., Asahi, K., Aoki, T., 2004. Timings and causes of glacial advances across the PEP-II transect (East-Asia to Antarctica) during the last glaciation cycle. Quat. Int. 118–119, 55–68. https://doi.org/10.1016/S1040-6182(03)00130-7.

Osada, K., Iida, H., Kido, M., Matsunaga, K., Iwasaka, Y., 2004. Mineral dust layers in snow at Mount Tateyama, Central Japan: formation processes and characteristics. Tellus B Chem. Phys. Meteorol. https://doi.org/10.3402/tellusb.v56i4.16436.

Ota, Y., Koike, K., Chinzei, K., Nogami, M., Machida, H., Matsuda, T., 2010. Geomorphology of the Japanese Islands. The University of Tokyo Press, p. 212 (in Japanese).

Poolton, N.R.J., Kars, R.H., Wallinga, J., Bos, A.J.J., 2009. Direct evidence for the participation of band-tails and excited-state tunnelling in the luminescence of irradiated feldspars. J. Phys. Condens. Matter 21, 485505. https://doi.org/10.1088/0953-8984/21/48/485505.

Reiners, P.W., Brandon, M.T., 2006. Using thermochronology to understand orogenic erosion. Annu. Rev. Earth Planet. Sci. 34, 419–466. https://doi.org/10.1146/annurev.earth.34.031405.125202.

Sanders, J.W., Cuffey, K.M., Moore, J.R., MacGregor, K.R., Kavanaugh, J.L., 2012. Periglacial weathering and headwall erosion in cirque glacier bergschrunds. Geology 40, 779–782. https://doi.org/10.1130/G33330.1.

Sato, H., 1994. The relationship between Late Cenozoic tectonic events and stress field and basin development in northeast Japan. J. Geophys. Res. Solid Earth 99, 22261–22274. https://doi.org/10.1029/94JB00854.

Sawagaki, T., Aoki, T., Hasegawa, H., Iwasaki, S., Iwata, S., Hirakawa, K., 2004. Late Quaternary glaciations in Japan. in: Ehlers, J., Gibbard, P.L.B.T.-D. in Q.S. (Eds.). Quaternary Glaciations Extent and Chronology. Elsevier, pp. 217–225. https://doi.org/10.1016/S1571-0866(04)80127-1.

Seki, K., Kanda, W., Ogawa, Y., Tanbo, T., Kobayashi, T., Hino, Y., Hase, H., 2015. Imaging the hydrothermal system beneath the Jigokudani valley, Tateyama volcano, Japan: implications for structures controlling repeated phreatic eruptions from an audio-frequency magnetotelluric survey. Earth Planets Space 67, 6. https://doi.org/10.1186/s40623-014-0169-8.

Shuster, D.L., Cuffey, K.M., Sanders, J.W., Balco, G., 2011. Thermochronometry Reveals Headward Propagation of Erosion in an Alpine Landscape. Science 332, 84–88. https://doi.org/10.1126/science.1198401.

Spencer, C.J., Danišík, M., Ito, H., Hoiland, C., Tapster, S., Jeon, H., McDonald, B., Evans, N.J., 2019. Rapid exhumation of earth's youngest exposed granites driven by subduction of an oceanic arc. Geophys. Res. Lett. 46, 1259–1267. https://doi.org/10.1029/2018GL080579.

Steer, P., Huismans, R.S., Valla, P.G., Gac, S., Herman, F., 2012. Bimodal Plio–Quaternary glacial erosion of fjords and low-relief surfaces in Scandinavia. Nat. Geosci. 5, 635–639. https://doi.org/10.1038/ngeo1549.

Sternai, P., Herman, F., Valla, P.G., Champagnac, J.D., 2013. Spatial and temporal variations of glacial erosion in the Rhône valley (Swiss Alps): insights from numerical modeling. Earth Planet. Sci. Lett. 368, 119–131. https://doi.org/10.1016/j.epsl.2013.02.039.

Sueoka, S., Tsutsumi, H., Tagami, T., 2016. New approach to resolve the amount of Quaternary uplift and associated denudation of the mountain ranges in the Japanese Islands. Geosci. Front. 7, 197–210. https://doi.org/10.1016/j.gsf.2015.06.005.

Sueoka, S., Tagami, T., 2019. Low-temperature thermochronological database of bedrock in the Japanese Islands. Isl. Arc 28, e12305. https://doi.org/10.1111/iar.12305.

Taira, A., 2001. Tectonic evolution of the Japanese Island Arc system. Annu. Rev. Earth Planet. Sci. 29, 109–134. https://doi.org/10.1146/annurev.earth.29.1.109.

Tanaka, S., Kagami, H., 1987a. Regional variation of Sr isotopic ratios in the Funatsugranitoids. MAGMA 80, 10–14 (in Japanese).

Tanaka, S., Kagami, H. (1987) Rb-Sr isotopic ages of the granitic rocks in the Tsurugidake-Kekachiyamaarea, northern Japan Alps. (in Japanese with English abstract).

Takahashi, M., 2006. Tectonic developments of the Japanese Islands controlled by Philippine Sea Plate Motion (in Japanese with English abstract). J. Geogr. 115, 116–123. https://doi.org/10.5026/jgeography.115.116.

Takehara, M., Horie, K., 2019. U–Pb zircon geochronology of the Hida gneiss and granites in the Kamioka area, Hida Belt. Isl. Arc 28, e12303. https://doi.org/10.1111/iar.12303.

Takeuchi, Y., Endo, Y., Murakami, S., 2008. High correlation between winter precipitation and air temperature in heavy-snowfall areas in Japan. Ann. Glaciol. 49, 7–10. https://doi.org/10.3189/172756408787814898.

Tarantola, A., 2005. Inverse Problem Theory and Methods for Model Parameter Estimation. Society for Industrial and Applied Mathematics.

Tomkin, J.H., Braun, J., 2002. The influence of alpine glaciation on the relief of tectonically active mountain belts. Am. J. Sci. 302, 169. https://doi.org/10.2475/ajs.302.3.169.

Wagner, G.A., Reimer, G.M., 1972. Fission track tectonics: the tectonic interpretation of fission track apatite ages. Earth Planet. Sci. Lett. 14, 263–268. https://doi.org/10.1016/0012-821X(72)90018-0.

Watanabe, T., 1989. Environmental factors influencing the landscape of the Kuranosuke Cirque, Tateyama Range, Northern Japanese Alps. Mt. Res. Dev. 9, 129–144. https://doi.org/10.2307/3673476.

Whipple, K.X., Kirby, E., Brocklehurst, S.H., 1999. Geomorphic limits to climate-induced increases in topographic relief. Nature 401, 39–43. https://doi.org/10.1038/43375.

Yamada, R., Sawada, H., Aoyama, S., Ouchi, W., Niki, S., Nagata, M., Takahashi, T., Hirata, T., 2021. Zircon U–Pb ages and whole–rock geochemistry from the Hida granites: implications for the geotectonic history and the origin of Mesozoic granites in the Hida belt, Japan. J. Mineral. Petrol. Sci. 116, 61–66. https://doi.org/10.2465/jmps.201125.

Yonekura, N., Kaizuka, S., Nogami, M., Chinzei, K., 2001. Regional geomorphology of the Japanese Islands. In: Introduction to Japanese Geomorphology, 1. University of Tokyo Press, Tokyo.

Yoshimura, C., Omura, T., Furumai, H., Tockner, K., 2005. Present state of rivers and streams in Japan. River Res. Appl. 21, 93–112. https://doi.org/10.1002/rra.835.

Zeitler, P.K., Meltzer, A.S., Brown, L., Kidd, W.S.F., Lim, C., Enkelmann, E., 2014. Tectonics and topographic evolution of Namche Barwa and the easternmost Lhasa block, Tibet. in: Hoke, D., Nie, Horton K. (Eds.). Toward an Improved Understanding of Uplift Mechanisms and the Elevation History of the Tibetan Plateau. Geological Society of America, pp. 23–58. https://doi.org/10.1130/2014.2507(02).